A novel fit-flexible fluorescence imager: Tri-sensing of intensity, fall-time, and life profile

Ali Taimori, Bethany Mills, Erin Gaughan, Aysha Ali, Kevin Dhaliwal, Gareth Williams, Neil Finlayson, and James Hopgood, *Senior Member, IEEE*

***Abstract*—Time-resolved fluorescence imaging techniques, like fluorescence lifetime imaging microscopy, are powerful optical instrumentation tools of modern science with important applications, including: biology, medicine, and chemistry. However, these systems possess complexities both at device and specimen levels due to their quantum-based nature, causing difficulties in quantifying biomarkers. To address the problem, we first aim to understand the underlying phenomena of fluorescence decay curves observed in our confocal imaging systems by deriving a flexible electrical model, paralleling similar approaches in the literature. A white-box model is presented for explaining the whole process as 'life circuits'. Components of excitation laser, specimen, and fluorescence-emission signal as the histogram of photon counts are modelled by a current source, network of RLC circuitry, and voltmetre, respectively. Solving the differential equation behind a life circuit results in a parametric 'life model' fitted with the real recordings. Then, we design a novel pixel-level temporal classification algorithm, called a 'fit-flexible approach', where qualities of 'intensity', 'fall-time', and 'life profile' are identified for each point. We provide a set of life models to select the best representative of the photon-counting histogram based on a new Misfit-percent criterion. Two-dimensional arrangement of the quantified information detects some kind of structural information. We improved 7% the Misfit error of recovering histograms on real samples than the best competitor. Our approach showed a potential of separating microbeads from the lung tissue, distinguishing the tri-sensing from conventional ones.**

***Index Terms*—Fluorescence lifetime imaging microscopy, lifetime estimation, modelling, system identification.**

I. Introduction

A. Time-resolved fluorescence imaging

FLUORESCENCE imaging techniques are a remarkable quantum-based piece of equipment with numerous applications across biology, chemistry, medicine, materials and environmental sciences [1]. In life sciences, the time-resolved technique of optical Fluorescence Lifetime Imaging Microscopy (FLIM) [2] or spectroscopy [3] are widely employed for microscopy or nanoscopy of biological substances. In FLIM, a specimen is first excited via a light source such as a laser. The reactional response to this excitation leads to photon absorption and emission. Then, the time of the first emitted photon is recorded by a sensitive detector, such as a single-photon avalanche diode sensor and related electronic equipment [4]. The cycle continues for a given number of excitation. At the end of process, a temporal histogram from counting photons in different time bins is produced. The mean lifetime, as a biomarker/chemomarker characteristic of the transient response, is estimated and utilised to bring a contrast among diverse locations in the sensed specimen [5–13].

This work was supported by EPSRC through the Healthcare Impact Partnerships, Grant Ref EP/S025987/1, "Next-generation sensing for human in vivo pharmacology- Accelerating drug development in inflammatory diseases".

A. Taimori and J. Hopgood are with the Institute for Digital Communications, School of Engineering, University of Edinburgh, Edinburgh EH9 3JL, UK (e-mail: ataimori@ed.ac.uk; James.Hopgood@ed.ac.uk).

B. Mills, E. Gaughan, A. Ali, K. Dhaliwal, and G. Williams are with the Centre for Inflammation Research, Edinburgh Medical School, University of Edinburgh, Edinburgh EH16 4TJ, UK (e-mail: beth.mills@ed.ac.uk; erin.gaughan@ed.ac.uk; aysha.ali@ed.ac.uk; kev.dhaliwal@ed.ac.uk; g.o.s.williams@ed.ac.uk).

N. Finlayson is with the Institute for Integrated Micro and Nano Systems, School of Engineering, University of Edinburgh, Edinburgh EH9 3FF (e-mail: n.finlayson@ed.ac.uk).

B. Background investigation

In the fluorescence techniques literature, the function representing time-resolved measurements from a photon counting process is considered as one of the decaying models of mono-, bi-, tri-, or generally multi-exponential [14]. For the most general infinite exponentials, the fluorescence decay curve is:

$$v(t) = \sum_{i=1}^{\infty} A_i e^{-\frac{t}{\tau_i}} = A \sum_{i=1}^{\infty} \alpha_i e^{-\frac{t}{\tau_i}}, \tag{1}$$

which $A_i \in \mathbb{R}^+$ and $\tau_i \in \mathbb{R}^+$, $\forall i$, denote the amplitude and the lifetime of i^{th} term, respectively. The symbol $\mathbb{R}^+$ denotes the set of all positive real numbers. There exist $A \triangleq \sum_{i=1}^{\infty} A_i$, $\alpha_i \triangleq \frac{A_i}{A}$, $0 < \alpha_i < 1$, $\forall i$, and $\sum_{i=1}^{\infty} \alpha_i = 1$. In conventional FLIM, the center of mass of the histogram of photon counts is determined as the fluorescence lifetime [3]. In (1), this is:

$$\tau_{\text{mean}} = \frac{\sum_{i=1}^{\infty} \alpha_i \tau_i^2}{\sum_{i=1}^{\infty} \alpha_i \tau_i}. \tag{2}$$

Its derivation is provided in Section S2 of Supplementary Materials (SMs). The histogram of photon counts is usually modelled by a mono-exponential due to its simplicity and applicability [6, 13]. A bi- or tri-exponential may be applied for complex materials [9, 15].

The time-resolved fluorescence signal in (1) is analysed as a black-box time series system modelling, where inputs are not observed and only the measured outputs as the histogram of photon counts are available [16]. This means a user is aware of the result of molecular reactions, but unaware of their detailed origin. This issue brings a profound gap to understanding physical concepts. Finding the origin differential equation satisfying (1), as a practice of grey-box modelling, reduces the opacity of the model. For mono-exponential, interpretations in terms of Jablonski diagram [17] and the 1^{st}-order

TABLE I: Terminology and definitions used in the paper

Terminology	Definition
Growth phase	The duration in a time series starting from the time zero to reaching the maximum intensity
Decay phase	The duration in a time series starting from the maximum intensity to the asymptotic dissipation
Life cycle	The sum of the growth phase and the decay phase
Life profile	The shape or envelope of a time series regardless of any growth or decay local fluctuations
Life model-set	A set of mathematical functions describing different time series
Life pattern map	An image arrangement of different life profiles in a 2D space visualised by distinct colours
Fall-time	The time at which a representative life profile falls $\frac{1}{e}$ its maximum intensity

Ordinary Differential Equation (ODE)[1] exist. However, there is a lack of research on interpretations for high-order models. Rare studies also exist beyond exponential. For example, the lack of a function other than the exponential for describing environments containing complex materials is identified in [18]. They modelled the decay as a gamma distribution for better experimental data fitting. Lukichev in [19] proposed the stretched exponential Kohlrausch-Williams-Watts (KWW) function $f(t) = Ae^{-\left(\frac{t}{\tau}\right)^{\gamma}}$, $0 < \gamma \leqslant 1$. This brings fitting closer to the physical decaying phenomena with time-varying ODEs than the mono-exponential with the integer exponent $\gamma = 1$ resulting from an ODE with constant coefficients [13]. That author suggested four circuits including resistor, capacitor, diode, and transistor to obtain some degree of flexibility. It is important to note that the fractional KWW system itself can be expanded via (1), aka Prony series expansion [20].

To estimate τ_{mean}, the unknown parameters of (2) should be estimated. Lifetime estimation methods can be categorised into three main groups: fitting-, non-fitting-based, and fit-free approaches. In fitting-based procedures, a decaying function is first hypothesised for modelling the distribution of the temporal signal. Then, its unknown parameters are estimated by approaches such as Least Squares (LS) curve fitting [21] or Maximum Likelihood Estimation (MLE) [5]. Non-fitting-based approaches usually suggest an explicit closed-form formulation for obtaining the fluorescence lifetime [6–9]. For example, Rapid Lifetime Determination (RLD) [6], RLD with Overlapping Windows (RLD-OW) [7], Robust RLD [13], Center of Mass Method (CMM) [8], and Fluorescence Lifetime Estimation via Rotational Invariance Techniques (FLERIT) [9] belong to this family. Fit-free methodologies rely on information visualisation [10] and learning [11, 15]. For instance, Digman et al. in [10] proposed a 2D graphical representation of mono- or bi-exponential lifetime distribution from FLIM pixels. This works based on a Fourier-domain-connected calculations called the "phasor approach". The method requires observer's interpretation. Also, fit-free machine learning-based techniques [11, 15] employ the inherent function approximation capability in neural networks to estimate parameters of a decay model by pre-training from massive synthetic data.

C. Problem statement

Let $f(t) = A\sum_{i=1}^{n} \alpha_i e^{-\frac{t}{\tau_i}}$ be a truncated representation of (1). Here, we aim to highlight the function $f(t)$ is the homogeneous solution of a n^{th}-order linear non-homogeneous ODE with constant coefficients [22]. Assume the input-output functions $e(t)$ and $f(t)$ represent the processes of excitation and fluorescence-emission, respectively. An equivalency between the radiation source and the rate of changes of the fluorescence emission exist, which describes a balanced input-output energy with the ODE of:

$$\frac{d^n f(t)}{dt^n} + a_1 \frac{d^{n-1} f(t)}{dt^{n-1}} + \cdots + a_{n-1} \frac{df(t)}{dt} + a_n f(t) = e(t), \quad (3)$$

in which $a_i, \forall i = 1, \ldots, n$, denotes a constant coefficient. The solution $f(t)$ is valid for a homogeneous ODE with $e(t) = 0$, where its corresponding characteristic function as $r^n + a_1 r^{n-1} + \cdots + a_{n-1} r + a_n = 0$ contains n distinct real roots of $r_1, r_2, \ldots, r_n$. So, the n-exponential would be able to articulate a decay function by combining linearly n segments. However, it should be noted that the roots can be generally of distinct real, repeated real and complex conjugate forms [18–20], resulting in different homogeneous solutions to be taken into account. A best practice in (3) would be to convert the ODE-based grey box to a transparent white box with fully identifiable components like an electrical circuit. Hence, the first question addressed in this research is: **"Q1: How can we represent the fluorescence phenomenon using white-box modelling?"**

Secondly, another problem with the methods developed in the literature is that they act based on only a presumed model; e.g., a fixed single model chosen from a small set such as mono- and bi-exponential is considered for describing the fluorescence phenomenon throughout a specimen [23]. However, different locations from a sample may not obey a given parametric model due to diversity of type, dynamics, and environment of biological substances present in the sample. This introduces modelling error. Therefore, the second question is: **"Q2: What model minimises curve fitting error on the real time-resolved measurements?"**

Thirdly, it is assumed that the intensity is maximum at the time $t = 0$ in both mono- and bi-exponential decay. This

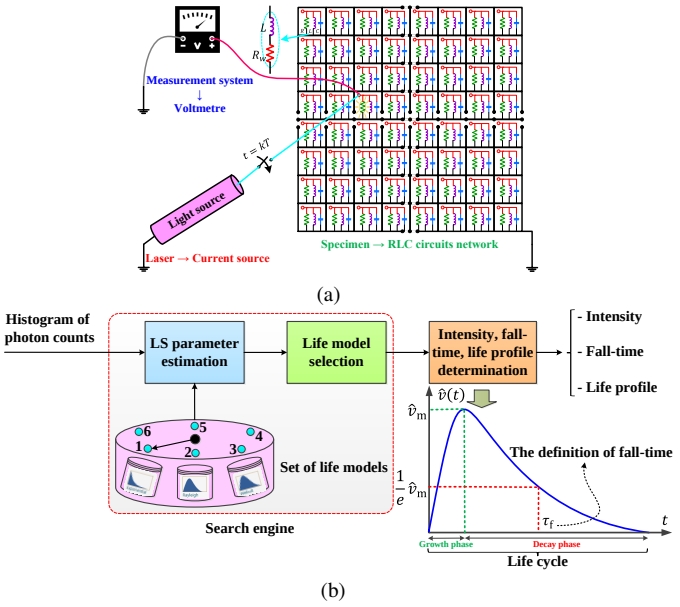

Fig. 1: (a) Modelling the whole process of time-resolved fluorescence imaging; and, (b) scheme of our fit-flexible imager.

[1]http://www.fluortools.com/software/decayfit/documentation/models

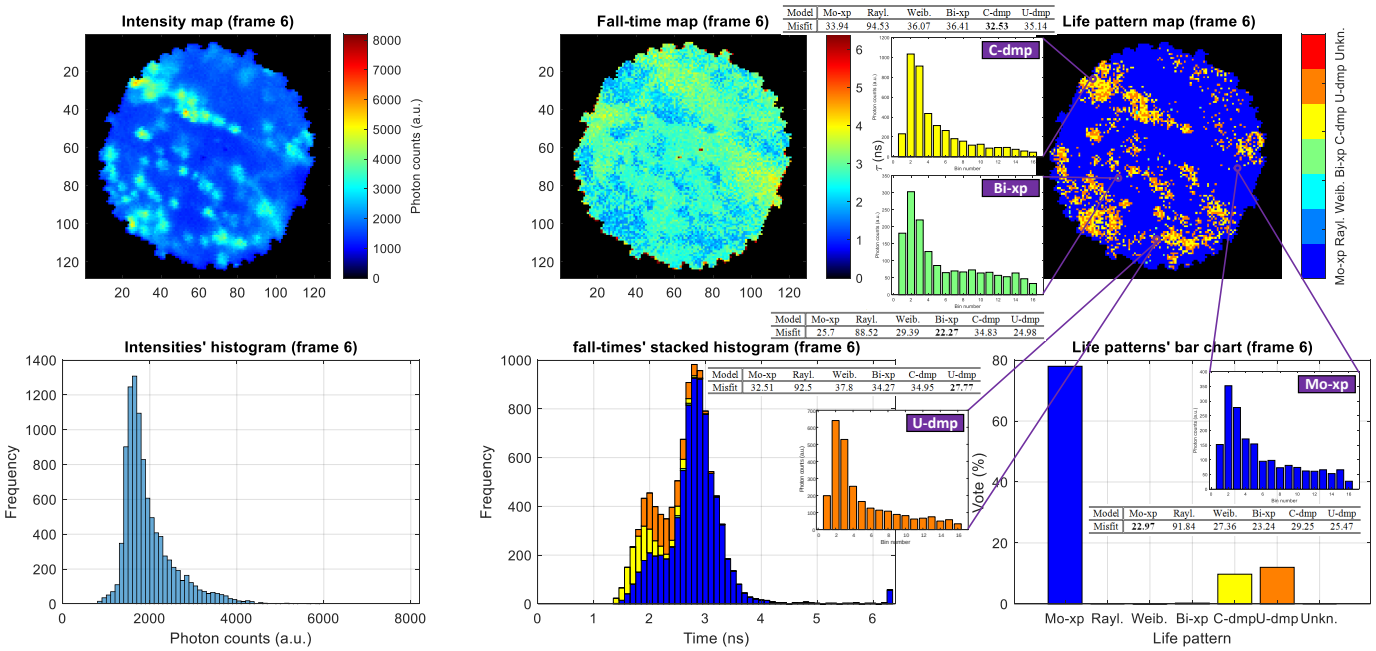

Fig. 2: A representation of the proposed fit-flexible fluorescence sensing for the application of time-resolved imaging of microscopic biological samples. On the right side, the histograms of photon counts at four distinct pixels are visualised. The table attached to each histogram shows the Misfit-percent for different models.

means an impulsive rise-time. However, because of natural lag in the physical systems, the response shape may not completely follow from a strictly monotonically decreasing trend. Although very small, it takes a time to the response reaches its maximum strength. In the literature, this behaviour is justified by convolution of the decay with an instrument response function [5, 11, 13]. Physically, the temporal response of fluorescence first follows a rise (called a "growth phase") and then a fall (called a "decay phase") trend similar to any charging and discharging events. We define a fluorescence "life cycle" as the sum of growth and decay phases. Nevertheless, if the tunable parameter of time bin width is selected sufficiently large, a strictly monotonically decreasing curve may be observed due to combining photons of neighbouring bins [4], preserving the importance of the models. The problem is in connection with the technological limitation on temporal resolution of sensing electronic devices (about few picoseconds in time-correlated single photon counting-based technique [24]). It prevents high resolution details of the rise-time or natural fluctuations of the time series. We define a fluorescence "life profile" as the shape or envelope of a time series regardless of any growth or decay local fluctuations. Our third research question is: **"Q3: If a set of life models is available, what criterion is the best for selecting the optimal descriptor?"**

D. Our approach and contributions

To tackle the problems of limited and rigid life model [18, 19, 23], we introduce a novel, fourth family of estimators termed a fit-flexible approach. This process is similar to model selection techniques used in statistical modelling and parameter estimation [25], but is extended to consider further physical constraints. To help motivate the models, we first build on the work in [19] and scale down the whole complex quantum process of time-resolved fluorescence imaging as an electric circuit by leveraging their analogy as will be discussed in Section II. Specimen's microorganisms are modelled as a network of parallel RLC circuits as shown in Fig. 1 (a). To detect matched profiles in connection to circuits' responses, we design a fluorescence "life model-set". We have considered 1^{st}- and 2^{nd}-order dynamical systems [26]. The benefits of these models are the low-order simplicity and the appropriate coverage of systems dynamics. We specifically derive life circuits where their responses lead to a few well-behaved statistical distributions that can fit different shapes of histogram of photo counts in practice. In a search mechanism, we select the optimal life model order and model type describing a spot of the specimen [25]. Each point selects its optimal representative model in an automatic and adaptive fashion. Once an optimal life model was selected, other markers can be estimated, e.g., a fluorescence "fall-time" to measuring the time at which a representative life profile falls $\frac{1}{e}$ its maximum intensity. This fall-time is equal to the lifetime of mono-exponential decay. We have proposed a generic Fall-time Determination Procedure (FDP). Figure 1 (b) visualises our scheme for tri-sensing of intensity, fall-time, and life profile. The flexible modelling results in definition of a novel concept called a fluorescence "life pattern map", which extracts a third map, in addition to intensity and fall-time/lifetime maps, by a pixel-level temporal classification algorithm. A life pattern map is generated by arranging extracted temporal profiles on the plane as a multi-colour visualisation. Table I summarises the terminology, and Fig. 2 represents the proposed imager.

Our experiments on the lung demonstrate quantifying both the fall-time as a stacked histogram in terms of models'

distribution and the life pattern map expose informative contrast among points. These act as complementary information about behaviour of a sample. It may be useful in discovering molecular and cellular structural information towards diseases treatment. Our contributions and novelties are:

- white-box modelling of the quantum-based imaging technique as an understandable electrical network, which may influence beyond the application of this paper;
- deriving a set of life circuits describing interactions between fluorophores and their environment;
- extracting life profile from time-resolved imaging;
- proposing a new $\mathrm{Misfit\text{-}percent}$ criterion for minimising modelling error in determination of life characteristics; and,
- applying our fit-flexible approach to real data for separating microbeads from human lung tissue.

In the remainder of paper, Section II electrically models the process of time-resolved imaging. Section III designs an algorithm for the proposed fit-flexible imager. In Section IV, we prepare both synthesised and actual experiments to validate our approach. The paper is finally concluded in Section V.

II. Electrical modelling

A. Excitation-emission modelling

When a specimen is excited, electrons of its excited molecules move from a ground state to an excited state and may or may not release photons of visible light and then come back to the base state [17]. Similarly, in a RLC circuit, after flowing periodic current, electrons in the circuit move to establish the fast events of charging and discharging. With this analogy, we desire to model the whole process electrically to give a physical interpretation for the theoretical models of photon counting. We use the pair of the current $i(t)$ and voltage $v(t)$ functions as representatives of the excitation $e(t)$ and fluorescence-emission $f(t)$ functions, respectively. It is also possible to equivalently describe the whole process as a mechanical system containing mass-spring-damper components or by bond graph theory [26]. However, electrical circuits have been chosen simply to reflect both the nature of electron movement and convenient means for physical interpretation of relaxation phenomena by inspiration from [19].

B. Specimen modelling

Modelling biological systems tries to understand real biochemical processes for goals such as synthesising artificial biological systems with similar functions. To model a specimen such as the lung tissue, we discretise the surface of the continuous sample into infinite extremely small units, each modelled by a RLC circuit excitable by an external laser. The light flow passes through the sample, introducing light reaction as photon emission, and heat and gas propagation as negligible absorption events. To electrically translate this, a spot of the specimen should contain both storage and load elements. A storing element, whether the capacitor C or the inductor L, is first charged by the incoming light and then discharged via an Ohmic load like a light bulb model as a representative of the resistor R [19]. Therefore, each unit of the sample is modelled by a linear, parallel RLC circuit.

C. Laser modelling

A pulsed laser, as an illumination source [27], generates short-duration focused light pulses [14]. It can be generally modelled by a current impulse train plus a DC shifter as:

$$i(t) = \underbrace{c_1 \sum_{k=0}^{K-1} \delta(t - kT)}_{\triangleq i_1(t)} + \underbrace{c_2 u(t)}_{\triangleq i_2(t)}. \tag{4}$$

Currents $i_1(t)$ and $i_2(t)$ model pure periodic laser impulses and a residual average power spread in-between the pulses as an imperfection, respectively. Operators $\delta(\cdot)$, $u(\cdot)$, and T denote the Dirac delta, Heaviside step function, and laser repetition rate, respectively. The arbitrary constants c_1 and c_2, and K respectively represent the amplitude of the impulse, the DC shift, and the number of excitation pulses per spot. In current lasers, the repetition rate is between nano- and microsecond range with thousands femtosecond pulse width [2].

D. Analogue electronic measurements modelling

The measurement equipment in time-resolved imaging can be modelled by an AC voltmetre recording a circuit's response. Figure 1 (a) embodies our modelling. We consider the capacitance of the capacitor as $C = 1$ F to meets the standard convention in (3) that the coefficient corresponding to the highest derivative order is unity [31]. A passive analogue RLC circuit is in nature a 2^{nd}-order system. Three possible over- (equivalent to bi-exponential), critically-, and under-damped responses exist based on the position of the roots of the characteristic equation [22]. We derive 2^{nd}-order circuits that solving their ODEs results in the definition of three proposed bi-exponential, critically-, and under-damped life models.

The real model of an inductor consists of its winding equivalent resistor of the resistance R_w series with the ideal inductor of the inductance L, as shown in Fig. 1 (a). So, if an inductor model inside a specimen's unit tend to $R_w \to \infty$, then, the RLC circuit reduces to a 1^{st}-order RC circuit. In this transition, we derive the most general Linear Time-Variant (LTV) RC circuit that its response lead to Weibull distribution as a flexible model considering both the growth and decay behaviours. Mono-exponential and Rayleigh models can be considered as special cases of Weibull's function with the integer time exponents $b = 1$ and $b = 2$ in Table II, respectively. Hence, they have established independently. Consequently, three models are derived from the 1^{st}-order modelling. Finally, 6 comprehensive 1^{st}- and 2^{nd}-order models constitute our life model-set. Table II summarises our developed life circuits, and Fig. 3 illustrates synthesised life profiles. Their corresponding functions can approximate well different shapes from histogram of photon-counts. We have motivated the choice of a set of life models are physically meaningful rather than an arbitrary choice of waveforms, as often seen in model selection problems. We have also spotted potential applications of life circuits for further follow-up among other fields. Section S3 from SMs provides proofs of life models.

TABLE II: A summary of our developed fluorescence life circuits

Model	Equivalent circuit	Components	Input/output equations	Specifications	Potential application areas
Mo-xp	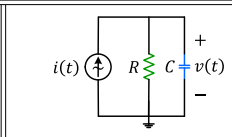	• $R = \tau$ • $C = 1$	• $i(t) = \frac{A}{K}\sum_{k=0}^{K-1}\delta(t-kT)$ • $v(t) = Ae^{-\frac{1}{\tau}t}u(t)$	• 1^{st}-order mono-exponential • Linear, time-invariant ODE • A pole at $s = -\frac{1}{\tau}$ • Equivalency among time constant, lifetime, and fall-time • A LTI translation of Weibull life model with $b = 1$ • Parameters: $\theta^{(1)} = [A, \tau]^{\mathrm{T}}$	• Biomedicine (fluorescence [13, 28]) • Chemistry (spectroscopy) • Nuclear science (radioactive decay)
Rayl.	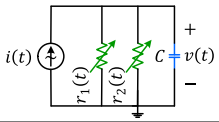	• $r_1(t) = \frac{\tau}{2t}$ • $r_2(t) = -t$ • $C = 1$	• $i(t) = \frac{A}{K}\sum_{k=0}^{K-1}\delta(t-kT)$ • $v(t) = Ate^{-\frac{1}{\tau}t^2}u(t)$	• 1^{st}-order Rayleigh • Linear, time-variant ODE [29] • A special Weibull circuit with $b = 2$ • Parameters: $\theta^{(2)} = [A, \tau]^{\mathrm{T}}$	• Medicine (MRI) • Life sciences • Wireless communications (fading modelling)
Weib.		• $r_1(t) = \frac{\tau}{bt^{b-1}}$ • $r_2(t) = \frac{t}{1-b}$ • $C = 1$	• $i(t) = \frac{A}{K}\sum_{k=0}^{K-1}\delta(t-kT)$ • $v(t) = At^{b-1}e^{-\frac{1}{\tau}t^b}u(t)$	• 1^{st}-order Weibull • Linear, time-variant ODE [29] • Flexibility • Parameters: $\theta^{(3)} = [A, b, \tau]^{\mathrm{T}}$	• Biomedicine [28] • Life sciences • Fading channels [30] • Reliability engineering
Bi-xp	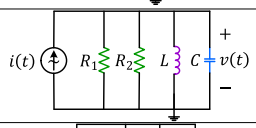	• $R_1 = \tau_1$ • $R_2 = \tau_2$ • $L = \tau_1\tau_2$ • $C = 1$	• $i(t) = \frac{A}{K}\sum_{k=0}^{K-1}\delta(t-kT) + A\left[\frac{\alpha}{\tau_2} + \frac{(1-\alpha)}{\tau_1}\right]u(t)$ • $v(t) = A\left[\alpha e^{-\frac{1}{\tau_1}t} + (1-\alpha)e^{-\frac{1}{\tau_2}t}\right]u(t)$	• 2^{nd}-order bi-exponential • Linear, time-invariant ODE • Real poles at $s_1 = -\frac{1}{\tau_1}$ and $s_2 = -\frac{1}{\tau_2}$ • Parameters: $\theta^{(4)} = [A, \alpha, \tau_1, \tau_2]^{\mathrm{T}}$	• Biomedicine (fluorescence imaging [28]) • Biochemistry [22] • Bioengineering
C-dmp	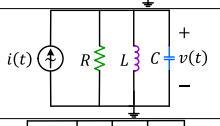	• $R = \frac{\tau}{2}$ • $L = \tau^2$ • $C = 1$	• $i(t) = Au(t)$ • $v(t) = Ate^{-\frac{1}{\tau}t}u(t)$	• 2^{nd}-order critically-damped • Linear, time-invariant ODE • Double pole at $s_{1,2} = -\frac{1}{\tau}$ • Parameters: $\theta^{(5)} = [A, \tau]^{\mathrm{T}}$	• Biomedicine (fluorescence imaging [28]) • Biochemistry [22] • Bioengineering
U-dmp	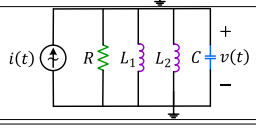	• $R = \frac{\tau}{2}$ • $L_1 = \tau^2$ • $L_2 = \frac{1}{\omega^2}$ • $C = 1$	• $i(t) = A\omega u(t)$ • $v(t) = Ae^{-\frac{1}{\tau}t}\sin(\omega t)u(t)$	• 2^{nd}-order under-damped • Linear, time-invariant ODE • Complex conjugate poles at $s_{1,2} = -\frac{1}{\tau} \pm j\omega$ • Needs rectifying $v(t)$ as (5) • Parameters: $\theta^{(6)} = [A, \omega, \tau]^{\mathrm{T}}$	• Biomedicine (fluorescence imaging [28]) • Biochemistry [22] • Bioengineering

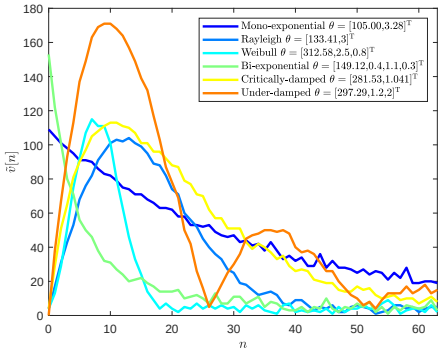

Fig. 3: An illustration of synthesised fluorescence life profiles.

III. Algorithmic Implementation

A. Real-world digital measurements

In actual measurements, the number of counted photons at each time bin of histogram of photon counts is a non-negative value [13]. This means that unquantised amplitudes of a circuit voltage response should satisfy the real constraint $v(t) \in \mathbb{R}^+$. If any deviations exist, the negative parts of the signal model should be treated by rectification. Specifically, the situation is seen for the sinusoidal response of under-damped model in Table II (See also Fig. 3 in [19].). This can be electrically interpreted as passing the response through a representative full-wave rectifier implementable by schemes two or four perfect diodes. Generally, the rectified response can be mathematically modelled by:

$$v(t) \leftarrow |v(t)|, \tag{5}$$

which $|\cdot|$ means absolute function. Hence, for under-damped model, the new assigned version of $v(t)$ is applied for parameters estimation. Additionally, photon counting is done in practice at discrete time bins. If variables Δ and N are respectively the bin width and the number of bins for a histogram, the discrete representation $v[n], \forall n = 0, 1, \ldots, N-1$, of the continuous response $v(t)$ can be generated by replacing t with $n\Delta$ in life models. An algorithmic implementation of our method, depicted in Fig. 1 (b), is summarised in Algorithm 1.

Algorithm 1 The proposed fit-flexible fluorescence imager

Inputs: The $\mathbb{Z}^{h\times w\times N}$ fluorescence tensor data including a time-resolved histogram $\tilde{\mathbf{v}} = [\tilde{v}_0, \tilde{v}_1, \ldots, \tilde{v}_{N-1}]^{\mathrm{T}}$ at each pixel $(r, c), \forall r = 0, 1, \ldots, h-1, c = 0, 1, \ldots, w-1$, and the M-element life model-set $\mathcal{M}$.
Outputs: Maps of intensity $\mathbf{\Lambda} = [\lambda_{r,c}] \in \mathbb{Z}^{h\times w}$, fall-time $\mathbf{\Psi} = [\psi_{r,c}] \in \mathbb{R}^{h\times w}$, life pattern $\mathbf{\Phi} = [\phi_{r,c}] \in \mathbb{Z}^{+^{h\times w}}$.
for $r \leftarrow 0, h-1$ **do**
  for $c \leftarrow 0, w-1$ **do**
    Acquire the histogram $\tilde{\mathbf{v}}$ belonging to point (r, c).
    for $j \leftarrow 1, M$ **do**
      Estimate $\hat{\boldsymbol{\theta}}^{(j)}$ in Table II for $\mathcal{M}\{j\}$ by LS fit.
      Recover $\hat{\mathbf{v}}^{(j)}$ in (7) by replacing parameters.
      Obtain Misfit-percent $e_j = e\left(\tilde{\mathbf{v}}, \hat{\mathbf{v}}^{(j)}\right)$ by (8).
    end for
    Compute $j^\star$ in (9).
    Estimate intensity by (11) as $\lambda_{r,c} \leftarrow \hat{I}$.
    Feed $\hat{\mathbf{v}}^{(j^\star)}$ to FDP to estimate fall-time $\psi_{r,c} \leftarrow \hat{\tau}_{\mathrm{f}}$.
    Initialise life profile label as $\phi_{r,c} \leftarrow j^\star$.
    Update the life profile label using penaliser.
    Assign unknown class where required.
  end for
end for

B. Stochastic modelling

Measurements in the real world are noisy, but not deterministic as modelled in Section II. This means the deterministic life model of $v[n] \in \mathbb{R}^+$ should be contaminated by a representative random component. Various dependent and independent noise sources from photon counting equipment and instrument ambient disturbances exist [13]. Their collective effect can be considered as additive noise by a Poisson distribution of $\eta[n] \sim \mathcal{P}(\lambda)$, in which the parameter $\lambda \in (0, \infty)$ denotes the mean rate of shot noise photons. Hence, actual measurements for each model can be rewritten as:

$$\tilde{v}[n] = \lfloor v[n] \rceil + \eta[n], \tag{6}$$

where $\tilde{v}[n] \in \mathbb{Z}^+$ and $\eta[n] \in \mathbb{Z}^+$. The symbol $\mathbb{Z}^+$ represents the set of all positive integers. The operator $\lfloor \cdot \rceil$ means round function to mimic physical quantised measurements.

C. Life-model's parameters estimation and selection

Consider the multi-parameter models in Table II as the set $\mathcal{M} \triangleq \{\text{Mo-xp}, \text{Rayl.}, \text{Weib.}, \text{Bi-xp}, \text{C-dmp}, \text{U-dmp}\}$. For the j^{th} model, parameters can be represented by the vector $\boldsymbol{\theta}^{(j)} = \left[\theta_0, \ldots, \theta_{K_j-1}\right]^{\mathrm{T}}$, where $K_j, \forall j = 1, 2, \ldots, M$, denotes the number of parameters of j^{th} model. Also, $M \triangleq |\mathcal{M}| = 6$ means the number of elements of the life model-set, where $|\cdot|$ represents the cardinality of a set. Our method can be expanded to other candidate models. The unknown parameters are identified from available measurements of histogram of photon counts. The problem can be formulated by a parameter estimator. We utilised the optimized nonlinear LS with the "trust region" algorithm [21] for estimating the unknown vector as $\hat{\boldsymbol{\theta}}^{(j)}$. Once the vector $\hat{\boldsymbol{\theta}}^{(j)}$ was determined for the j^{th} model, its related fitted curve can be calculated by replacing the estimated parameters into its corresponding discrete response, definable as the vector of:

$$\hat{\mathbf{v}}^{(j)} = \left[\hat{v}_0^{(j)}, \ldots, \hat{v}_{N-1}^{(j)}\right]^{\mathrm{T}}. \tag{7}$$

Afterwards, our method contains a mechanism of model selection [23] below.

Misfit-percent *criterion:* To select an optimal curve describing the best data trend, various Badness-of-Fit (BoF) or Goodness-of-Fit (GoF) objective functions may be employed. Generally, BoF criteria such as two-sample Kolmogorov-Smirnov (K-S) difference [32], Kullback-Leibler (K-L) divergence [33], chi-square [13], Mean Squared Error (MSE) [13], Normalised Root Mean Square Error (NRMSE) [34] and Symmetric Mean Absolute Percentage Error (SMAPE) [35], or GoF Correlation Coefficient (CC) [33] can be used. However, these metrics suffer from two main problems: 1) being limited in terms of fidelity and robustness, or 2) being non-fully normalised. The former causes inefficient model selection in noisy situations; e.g., MSE may only work well for head (bins with higher intensities) fitting of the skewed life distributions, whereas the chi-square measure is loyal more to tail fitting [13]. The latter hardens understanding the rate of a criterion; e.g., consider the task of thresholding on a non-normalised value, which would not be straightforward by user. To tackle them, we have proposed a novel, simple yet efficient error metric for model selection, called Misfit-percent. This calculates the sum of absolute error between the actual histogram of photon counts and an estimated curve on all bins and normalise the result to the union of the curves as the whole possible photons space. Generally, Misfit between the actual $\mathring{\mathbf{p}}$ and estimated $\hat{\mathbf{p}}$ vectors is defined in $\%$ as:

$$\text{Misfit-percent} \triangleq \frac{100 \sum_{i=0}^{N-1} |\mathring{p}_i - \hat{p}_i|}{\sum_{i=0}^{N-1} \max(\mathring{p}_i, \hat{p}_i)}. \tag{8}$$

We redefine the entry $e\left(\tilde{\mathbf{v}}, \hat{\mathbf{v}}^{(j)}\right), \forall j = 1, 2, \ldots, M$, as the error of Misfit-percent between the vectors of actual histogram $\tilde{\mathbf{v}} = [\tilde{v}[0], \ldots, \tilde{v}[N-1]]^{\mathrm{T}}$ and j^{th} estimated model $\hat{\mathbf{v}}^{(j)}$ and arrange it over all models as $\mathbf{e} = \left[e\left(\tilde{\mathbf{v}}, \hat{\mathbf{v}}^{(1)}\right), \ldots, e\left(\tilde{\mathbf{v}}, \hat{\mathbf{v}}^{(M)}\right)\right]^{\mathrm{T}}$. The label of optimal life model for a single point can be detected by minimising:

$$j^{\star} = \arg\min_{j}(\mathbf{e}). \tag{9}$$

The minimised Misfit-percent model is refereed to intensity and fall-time estimators as well as life profile detection.

D. Intensity estimation

A summation on bin-wise photons is considered as intensity per histogram in FLIM [2] (called an "empirical mode") as:

$$\hat{I} = \sum_{i=0}^{N-1} \tilde{v}_i = \mathbf{1}^{\mathrm{T}} \tilde{\mathbf{v}}, \tag{10}$$

which $\mathbf{1}$ denotes a column-wise vector of all ones. Although this sort of integration has inherent smoothing property, the intensity still is calculated from a mixture of signal and noise. To improve SNR, we ideally desire to estimate the intensity from the original signal alone, i.e., $\hat{I} = \mathcal{G}(\tilde{\mathbf{v}})$, where the operator $\mathcal{G}(\cdot)$ is a denoiser. The denoising operator can be a non-parametric smoothing filter such as Savitzky-Golay filter [13] (called a "smoothed mode"), or a parametric fitting model (called a "fitted mode", as our approach is a type of this). If the function $\mathcal{G}$ is $\mathbf{1}^{\mathrm{T}}$, it is equivalent to (10). We leverage the capability of our life recovery to estimate the intensity. If Misfit stays below the fitting failure threshold T_{AM}, we rely on the integral of optimal fitted curve as a filtered, smoothed signal; otherwise, it is estimated as usual, as:

$$\hat{I} = \begin{cases} \mathbf{1}^{\mathrm{T}} \hat{\mathbf{v}}, & e\left(\tilde{\mathbf{v}}, \hat{\mathbf{v}}^{(j^{\star})}\right) < T_{\text{AM}} \\ \mathbf{1}^{\mathrm{T}} \tilde{\mathbf{v}}, & \text{otherwise} \end{cases}. \tag{11}$$

In experiments, we adjusted $T_{\text{AM}} = 10\%$. This mechanism can balance better between bias and variance.

E. Fall-time determination procedure

Conventional FLIM assumes a monotonically decaying curve, whereas underlying life distributions may be generally left or right skewed, or even symmetric. A skewed distribution has three characteristics of mode (its peak point), median, and mean (also defined as centre of mass [8] or the first moment). For possessing a right imaging system, distinguishing them is crucial. To this intent, we have measured fall-time as

graphically explained in Fig. 1 (b). The value of distributions characteristics can be determined mathematically or computationally. The former requires to analytically derive an equation for each life mode as a function of model parameters as presented in Table II. If during the fitting process, a failure in estimating one or more parameters exists due to lack of control on noisy data, computations are wrong, physically meaningless. For example, a lower bound for bi-exponential fall-time in terms of parameters (α, τ_1, τ_2) is:

$$\tau_{\mathrm{f}} \geqslant \frac{(1-\frac{1}{e})\tau_1\tau_2}{(1-\alpha)\tau_1+\alpha\tau_2}, \tag{12}$$

where it is derived in Section S4 of the SMs. However, in the latter, the parameter τ_{f} can be graphically computed from profile's shape with less sensitivity to parameters (α, τ_1, τ_2).

As seen from the curve of Fig. 1 (b), at most two points cross the red line corresponding to the amplitude $\frac{1}{e}\hat{v}_{\mathrm{m}}$, one corresponding to the rising edge, and one due to the falling edge. The estimated fall-time, $\hat{\tau}_{\mathrm{f}}$, is determined at falling edge of the response, i.e., the vertical green line. To analyse the intersection point for a given life model, we calculate slope at crossing points. For the rising and falling edges, the slope is identified respectively positive and negative. Nevertheless, for a measurement window, it may happen that such a crossover does not exist in the falling edge, for example, because of slow damping. In this case, we quantise the fall-time to a predefined span value such as $\hat{\tau}_{\mathrm{f}} = \Delta N$. In terms of estimated parameters, the profile of a fitted model may not always follow from a reasonable shape such as the first growth and then decay trend shown in the curve of Fig. 1 (b). Generally, five main possible rise and fall forms may occur in real scenarios, which are controlled in FDP of Algorithm 1 for obtaining $\hat{\tau}_{\mathrm{f}}$. Section S5 from SMs provides details of these cases. It is notable that, for the fall-time determination in U-dmp model, the envelope of the rectified sinusoidal response, namely $v(t) \leftarrow Ae^{-\frac{1}{\tau}t}u(t)$, is fed as input. Although the valid $\hat{v}_{\mathrm{m}}$ is calculated from the original rectified version in (5).

F. Life profile extraction

A decision about detecting fluorescence life profile can be selecting the model with minimum $\mathrm{Misfit\text{-}percent}$ in (9). Due to following reasons, this alone will not lead to accurate outcomes. A model from a "model set" may have different shapes. For the model, infinite "model parameters" can be imagined. In practice, mathematical functions from the model set may meet each other on some specific vectors of parameters, and consequently generate similar functional forms [36]. In our model set, it can be seen between the naturally flexible model of Weibull and other models. As clear examples, see specifications of mono-exponential and Rayleigh models in Table II. This reveals further rules are required to investigate model parameters and improve the chance of deciding a right profile. We check consistency of estimated parameters with physical constraints such as those mentioned in (1) and stability criterion. If we observe any inconsistencies, the corresponding model is penalised to be able to select the best descriptive label for a life profile. To this intent, consider the matrix of fluorescence life pattern map as $\mathbf{\Phi} = [\phi_{r,c}]_{h\times w}, \forall \phi_{r,c} \in \mathbb{Z}^+$. We first initialise $\phi_{r,c} \leftarrow j^\star$. Then, the entry $\phi_{r,c}$ is updated using a penaliser if necessary. In addition to the parameters control mechanism, we considered a parsimonious strategy in establishing penalising rules; namely, if the difference of $\mathrm{Misfit\text{-}percent}$ between two models is less than a threshold, a 1^{st}-order system is preferred than a 2^{nd}-order one. We set the rules according to our optimisation procedure. Nonetheless, important rules that may change the current state of a fluorescence life profile in (9) are itemised and detailed in Section S6 from SMs. Each label is coded by a distinct colour in software for visualisation. We have also defined an extra "unknown class" for more control on uncertainty in the proposed profile detection as expressed in Section S7 from SMs.

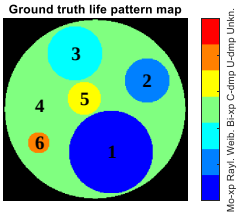

Fig. 4: Ground truth life pattern map in simulator.

IV. Experiments

A. Evaluation of imaging on synthetic samples

1) Synthesised-data generation and visualisation: We have generated synthetic data for simulation of sensing biological specimens based on a fibre bundle-based imager. Figure 4 depicts the ground truth image of a synthesised life pattern map. As shown in the colour bar of Fig. 4, each colour represents an individual life model. The histogram of photon counts for each pixel are obtained using the generative model in (6). Figure 3 plots the shape of life profiles at 6 separate locations of the fluorescence life regions in Fig. 4 from a random run. Section S8 from SMs explains setting of the number of photons per histogram for a model. We added Poisson noise with the rate $\lambda = 4$. The vectors of parameters of models are reported in the legend. Other parameters are: $N = 64$, $\Delta = 0.1$ ns.

Figure 5 visualises our imaging framework (See also Fig. S3 from SMs that visualises $\mathrm{Misfit\text{-}percent}$ error.). The representation contains an interesting example with the following two cases:

- Case I: Weib. and Bi-xp share the same intensity but different fall-times. These are respectively equivalent to the numbered regions 3 and 4 in Fig. 4. As seen in Fig. 5, the regions are not separable in the intensity map. Instead, the fall-time map reveals the differences. This proves the fact that time-resolved fluorescence fall-time/lifetime imaging surpasses steady state intensity sensing.
- Case II: As a generalised case, Mono-xp and C-dmp models respectively corresponding to the numbered regions 1 and 5 in Fig. 5, expose both the same intensity and fall-time but

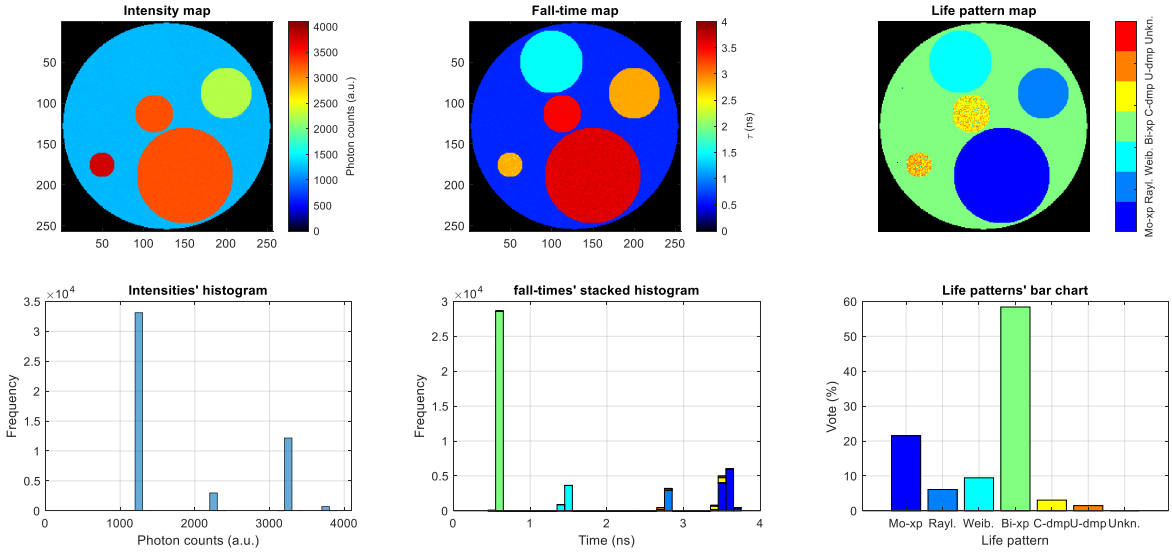

Fig. 5: Visualisation of our imager. This shows both the regions discriminability of Weib. and Bi-xp in Fall-time map (Case I), and Mo-xp and C-dmp in Life pattern map (Case II).

TABLE III: Efficiency of intensity and fall-time estimators

Model	Intensity (a.u.)		Fall-time (ns)	
	GT	$(\mu \pm \sigma)$	GT	$(\mu \pm \sigma)$
Mono-exponential	3000	3256±15.95	3.38	3.61±0.05
Rayleigh	2000	2255±16.29	2.69	2.83±0.01
Weibull	1000	1257±15.92	1.4	1.51±0.01
Bi-exponential	1000	1249±16.71	0.6	0.64±0.01
Critically-damped	3000	3250±15.93	3.38	3.5±0.02
Under-damped	3500	3758±17.72	2.73	2.78±0.07

different life profiles. Neither the intensity map nor the fall-time map cannot discriminate. However, they are separated in the life pattern map. This demonstrates the added value of our proposed life profile sensing, providing complementary information for high-level interpretations.

The visualisation contains 6 subplots, where from top to bottom and left to right include respectively: maps of intensity, fall-time and life pattern, intensities' histogram, a stacked histogram of fall-times that accounts for the distribution of each life model across time bins, and a bar chart which represents models portion in percent. A fall-times' stacked histogram can generally provide multi-modal distributions that make our model attractive for higher level analyses such as segmentation by valley thresholding. For instance, see the valley at $t \approx 2.3$ ns between the two peaks in the fall-times' stacked histogram of Fig. 2. The pixel-wise classification capability of life pattern map can reveal microscopic structures of a specimen. It provides complementary contrast information as coherent shapes such as distinct islands. The information can also be employed in other tasks like co-registration, fluorescence data classification, and image-to-image translation.

2) Bias and variance of estimating intensity and fall-time: Bias and variance are two metrics for measuring efficiency of an estimator as indicators of accuracy and precision, respectively. Table III reports mean and standard deviation of estimated intensity and fall-time values for different regions of

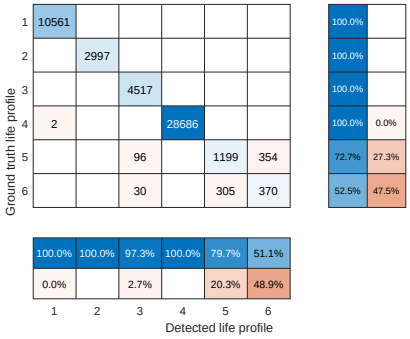

Fig. 6: The chart of confusion matrix of life profile detection.

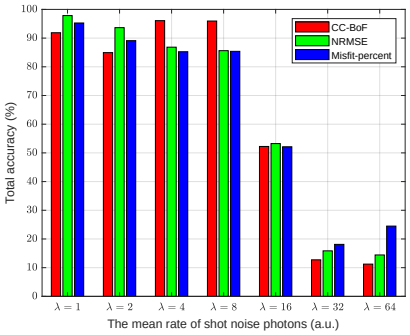

Fig. 7: Comparison of three error percentage criteria, including the proposed Correlation Coefficient-based and Misfit metrics.

Fig. 5. Ground truth information was calculated from the computational procedure described in Section III-E in the noiseless case. Comparing ground truth values to estimated intensity and fall-time results notifies acceptable overestimation levels in bias under controlled variances for all life models.

3) Confusion table of life profile detection: Here, for a more comprehensive evaluation of the proposed method, in addition to the parameters set marked in Fig. 3 (called The Parameters

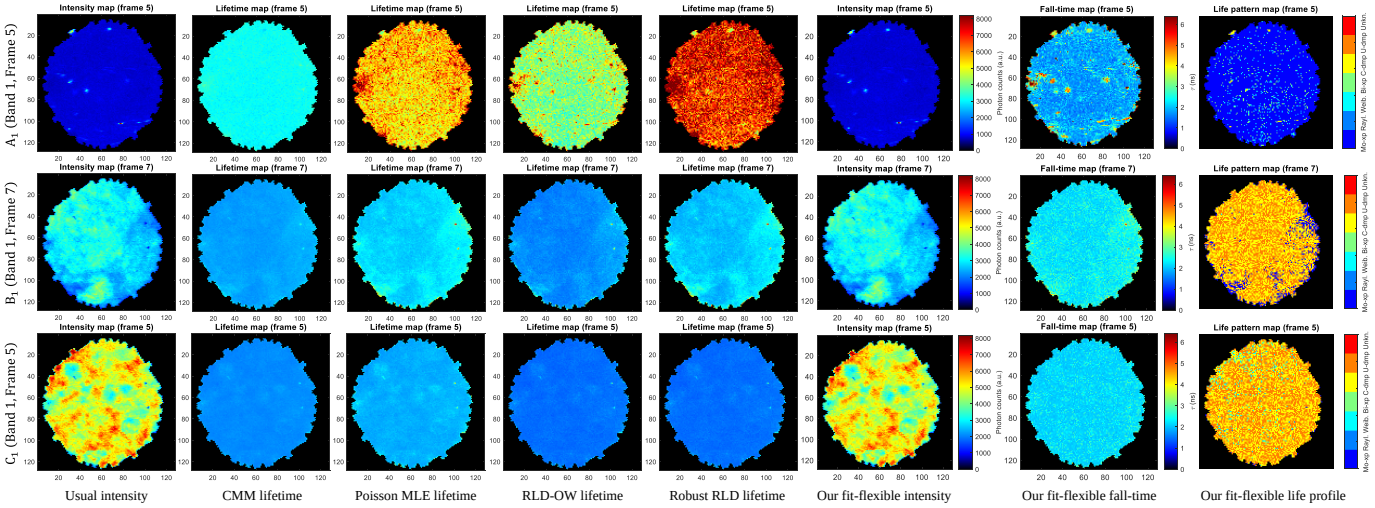

Fig. 8: Qualitative comparison of outputs of different approaches. Colour bars of corresponding maps have the same scale. The points with cyan colour in the Life pattern map from Sample C_1 reveal the locations of microbeads.

TABLE IV: Characteristics of the human lung experiment

Sample	Label	Probe/dye (relative intensity)	Shutter open	N_{f}	BoI†
Beads in saline	A_1	InSpek$^{\mathrm{TM}}$/Green (0.3 %)	Blue	12	1
Beads in saline	A_2	Sphero$^{\mathrm{TM}}$/Red (low)	Blue, orange	18	1, 2
The lung alone	B_1	-	Blue	17	1
The lung alone	B_2	-	Blue, orange	15	1, 2
The lung+beads	C_1	InSpek$^{\mathrm{TM}}$/Green (0.3 %)	Blue	19	1
The lung+beads	C_2	Sphero$^{\mathrm{TM}}$/Red (low)	Blue, orange	15	1, 2

† BoI stands for spectral Band(s) of Interest in investigation.

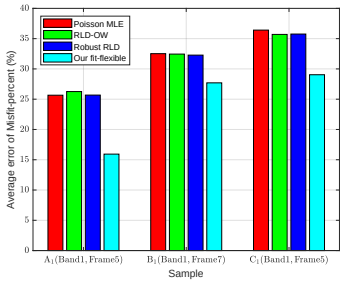

Fig. 9: Comparison of average histogram recovery error.

Set 1), we designed three other parameters sets resulting in diverse profiles. Section S9 from SMs provides details of The Parameters Sets 2 to 4. The confusion matrix of life profile detection for The Parameters Set 1 has reported in the core table of Fig. 6. For classes 1 to 3 and almost class 4 (with only 2 misclassified pixels as mono-xp), the classification is perfect. However, more misclassification errors mainly between classes 5 and 6 are seen as is confirmed in the upper right image of Fig.5. The origin of errors is the similarity of their estimated distributions. A number of pixels of individual classes of 5 and 6 had been misclassified as class Weib. as well. The side vertical and horizontal tables in Fig. 6 reports recall (accuracy) and precision per class, respectively. Empty cells mean 0. Total accuracy of life profile detection is 98.4%, 63.89%, 85.25%, and 97.07% for The Parameters Sets 1 to 4, respectively, which demonstrate reproducibility of results over the diversity of profiles' shapes and parameters. Averaging on all sets gives promising 86.15% accuracy.

4) Fidelity and robustness of Misfit-percent *criterion:* This section has devoted to investigate how the criteria stays stable by increasing noise levels. Due to the two problems mentioned about criteria, we have compared Misfit-percent to a proposed CC-based BoF metric and NRMSE $\triangleq \frac{100\|\hat{\mathbf{p}}-\mathring{\mathbf{p}}\|}{\|\hat{\mathbf{p}}-\mathrm{mean}(\mathring{\mathbf{p}})\|}$. The symbol $\|\cdot\|$ means l_2-norm. We used the NRMSE version implemented in MATLAB's System Identification Toolbox [34]. However, the correlation, as a GoF criterion with the ratio $-1 \leqslant r \leqslant 1$, cannot be directly employed in our framework, because of using the error percentage rate. To overcome the issue, we converted it back into a BoF metric, normalised between 0 and 100 percent defined as: CC-BoF $\triangleq 50(1-r)$. Figure 7 plots total accuracy of life profile detection for different approaches vs various noise levels with mean rates of $\lambda = 1, 2, 4, 8, 16, 32, 64$ on The Parameters Set 3. Misfit exposes competitive results with stable behaviour across rates. In intense noises of $\lambda = 32, 64$ that spike outliers appear, our criterion outperforms others. Our proposed Misfit-percent acts as a specific type of l_1-norm and remains outlier-robust in comparison to l_2-norm counterparts.

B. Test of imaging on real samples

1) Experimental samples preparation: To prove the concept of our approach in real imaging, we established a human lung experiment for acquiring samples that potentially meet desirable characteristics like diversity among samples, natural heterogeneity in life model, and the presence of 2D structural information. Data were collected *via* fibre-based time-resolved fluorescence imaging from an *ex vivo* human lung model [2], with the alveolar space spiked with fluorescent microspheres as a surrogate for fluorescently labelled bacteria. This was designed as an experimental mimic of recently reported optical endomicroscopy based imaging of cases of suspected ventilator associated pneumonia in a clinical setting [37]. A challenge in its data is the spectral overlap between the labelled bacteria and lung autofluorescence, limiting the imaging sensitivity. We

estimated fluorescence intensity, fall-time, and life profile to determine whether additional features could be identified with our approach than the steady-state intensity imaging.

All experimentation using human samples were performed following approval of the appropriate Regional Ethics Committee (REC), NHS Lothian, and the South East Scotland Research Ethics Committee 02 (reference 11/SS/0103), and with informed consent. The human lung was obtained from a solid organ donor after being declined by all UK transplant centers as being unsuitable for transplantation. The lung was prepared and ventilated as described in [38]. InSpek$^{\text{TM}}$ Green ($\lambda_{\text{ex}} = 505$ nm, $\lambda_{\text{em}} = 515$ nm) 6 μm Beads, 0.3 % intensity (ThermoFisher, I14785), and Sphero$^{\text{TM}}$ 1.7-2.2 μm Fluorescent Purple Particles ($\lambda_{\text{ex}} = 590$ nm, $\lambda_{\text{em}} = 620$ nm), low intensity (Sphero$^{\text{TM}}$ Tech, FL-2062-2) were each diluted 1:10 into sterile 0.9 % NaCl (Baxter). an amount 100 μL of each dilution was instilled to a defined region of the lung by needle and syringe, and imaging was performed by bespoke FLIM system and endoscopy imaging fibre described in [2, 13, 38]. Also, an amount 100 μL of the prepared beads in saline were imaged under the same parameters. We fed samples to our imager as well as conventional FLIMs.

2) Samples' imaging, outcomes and comparison: Data were captured with an image size of 128×128 pixels, 85 μs acquisition time per pixel, and 16 time bins. Laser excitation was at 480 nm and 590 nm, with collection in green (Band 1: $498 \sim 570$ nm) and red (Band 2: $594 \sim 764$ nm) spectral bands. Each sample contains N_{f} video frames. Figure S16 in SMs shows a data format of our imager. Table IV summarises information and acquisition data regarding the samples.

Figure 8 visualises outputs of our imager and compares them to methods of CMM [8], Poisson MLE [5], RLD-OW [7], and Robust RLD [13]. A visual comparison between usual and fit-flexible intensity maps justifies the expected Signal-to-Noise Ratio (SNR) improvement in our method. Also, our fall-time maps provide sharper and crisper images representing local variations than those of compared lifetime maps. To compare results of Fig. 8 more quantitatively, Fig. 9 reports average error of recovering histogram of photon counts calculated via (8). The proposed approach achieves the lowest error on all samples with around 7% improvement on average than the best competing result from Robust RLD, as a benefit of our model selection mechanism. The CMM approach was omitted from comparisons list; because, it only estimates the lifetime but not the amplitude of mono-exponential and consequently incapable of a full histogram recovery [13]. The distinguishable granular points on Samples A_1 and C_1 (places with beads' presence) show flow traces of microbeads on both saline and more importantly human lung tissue, which are not detectable by conventional systems of FLIM[2]. Figure S2 from SMs shows results of Sample C_1 after assigning an unknown class for segmenting foreground beads. This ability of discriminating beads from tissue can find attractive potential applications such as detection of microplastics in the lung, drug carriers efficacy, and bacteria detection.

[2]This problem is similar to the proverb "finding a needle in a haystack".

V. Conclusion and future studies

This paper first proposed a model for investigation of time-resolved fluorescence imagers. We modelled the complex quantum systems by understandable white-box electrical models. Afterwards, we derived life models for fluorescence techniques and beyond. Then, an algorithm called a fit-flexible approach, was developed for sensing fluorescence intensity, fall-time and life profile from hardware time-resolved imaging. Supported by the mathematical insights, we demonstrated capabilities of our method to visualising the information. Experiments on real data demonstrated sharper images and the potential for discriminating beads.

Our modelling can open up research avenues towards characterising molecular and cellular structures of living organisms. It would be of great importance in real-world scenarios because of potential applications to disease diagnosis and drug discovery. Due to the capabilities of stacked fall-time histogram and life profile detection, our approach can be employed in higher level biomedical images analysis tasks such as registration, segmentation and classification. One can also extend the search engine to more useful mathematical models describing real phenomena. Additionally, it is possible to extract other temporal markers from our framework such as the fluorescence rise-time. Other future developments could be incorporating spatial and spectral correlations.

References

[1] S. Trautmann *et al.*, "Fluorescence lifetime imaging (FLIM) in confocal microscopy applications: An overview," *PicoQuant GmbH*, vol. 29, p. 12489, 2013.

[2] G. O. Williams *et al.*, "Full spectrum fluorescence lifetime imaging with 0.5 nm spectral and 50 ps temporal resolution," *Nat. Commun*, vol. 12, no. 1, pp. 1–9, 2021.

[3] J. R. Lakowicz, *Principles of fluorescence spectroscopy*, 3rd ed. Springer, 2006.

[4] A. T. Erdogan *et al.*, "A CMOS SPAD line sensor with per-pixel histogramming TDC for time-resolved multispectral imaging," *IEEE J. Solid-State Circuits*, vol. 54, no. 6, pp. 1705–1719, 2019.

[5] A. Chessel *et al.*, "A maximum likelihood method for lifetime estimation in photon counting-based fluorescence lifetime imaging microscopy," in *IEEE* 21st *Eur. Signal Process. Conf.*, 2013, pp. 1–5.

[6] R. M. Ballew and J. Demas, "An error analysis of the rapid lifetime determination method for the evaluation of single exponential decays," *Anal. Chem.*, vol. 61, no. 1, pp. 30–33, 1989.

[7] K. K. Sharman *et al.*, "Error analysis of the rapid lifetime determination method for double-exponential decays and new windowing schemes," *Anal. Chem.*, vol. 71, no. 5, pp. 947–952, 1999.

[8] D. U. Li *et al.*, "Video-rate fluorescence lifetime imaging camera with CMOS single-photon avalanche diode arrays and high-speed imaging algorithm," *J. Biomed. Opt.*, vol. 16, no. 9, p. 096012, 2011.

[9] H. Yu *et al.*, "Estimation of fluorescence lifetimes via rotational invariance techniques," *IEEE. Trans. Biomed. Eng.*, vol. 63, no. 6, pp. 1292–1300, 2015.

[10] M. A. Digman *et al.*, "The phasor approach to fluorescence lifetime imaging analysis," *Biophys. J.*, vol. 94, no. 2, pp. L14–L16, 2008.

[11] J. T. Smith *et al.*, "Fast fit-free analysis of fluorescence lifetime imaging via deep learning," *Proc. Natl. Acad. Sci. U.S.A.*, vol. 116, no. 48, pp. 24 019–24 030, 2019.

[12] S. P. Chan *et al.*, "Optimized gating scheme for rapid lifetime determinations of single-exponential luminescence lifetimes," *Anal. Chem.*, vol. 73, no. 18, pp. 4486–4490, 2001.

[13] A. Taimori *et al.*, "Fast and robust single-exponential decay recovery from noisy fluorescence lifetime imaging," *IEEE. Trans. Biomed. Eng.*, vol. 69, no. 12, pp. 3703–3716, 2022.

[14] D. M. Jameson *et al.*, "The measurement and analysis of heterogeneous emissions by multifrequency phase and modulation fluorometry," *Appl. Spectrosc. Rev.*, vol. 20, no. 1, pp. 55–106, 1984.

[15] D. Xiao *et al.*, "One-dimensional deep learning architecture for fast fluorescence lifetime imaging," *IEEE J. Sel. Top. Quantum Electron.*, vol. 27, no. 4, pp. 1–10, 2021.
[16] L. Ljung, *System identification: Theory for the user*, 2nd ed. Prentice-Hall, Inc., 1999.
[17] M. Y. Berezin and S. Achilefu, "Fluorescence lifetime measurements and biological imaging," *Chem. Rev.*, vol. 110, no. 5, pp. 2641–2684, 2010.
[18] J. Włodarczyk and B. Kierdaszuk, "Interpretation of fluorescence decays using a power-like model," *Biophys. J.*, vol. 85, no. 1, pp. 589–598, 2003.
[19] A. Lukichev, "Physical meaning of the stretched exponential kohlrausch function," *Phys. Lett. A*, vol. 383, no. 24, pp. 2983–2987, 2019.
[20] A. Lattanzi *et al.*, "Physics and mathematics of the photoluminescence of complex systems," *arXiv:2012.04645v2*, 2021.
[21] A. R. Conn *et al.*, *Trust region methods*. SIAM, 2000.
[22] S. Iotti *et al.*, "The mono-exponential pattern of phosphocreatine recovery after muscle exercise is a particular case of a more complex behaviour," *Biochim Biophys Acta Bioenerg*, vol. 1608, no. 2-3, pp. 131–139, 2004.
[23] M. I. Rowley *et al.*, "Robust Bayesian fluorescence lifetime estimation, decay model selection and instrument response determination for low-intensity FLIM imaging," *PLoS One*, vol. 11, no. 6, p. e0158404, 2016.
[24] C. Liu *et al.*, "Timing and operating mode design for time-gated fluorescence lifetime imaging microscopy," *Sci. World J.*, 2013.
[25] P. Stoica and Y. Selen, "Model-order selection: A review of information criterion rules," *IEEE Signal Process. Mag.*, vol. 21, no. 4, pp. 36–47, 2004.
[26] H. M. Paynter, *Analysis and design of engineering systems*. MIT press, 1961.
[27] W. Shi *et al.*, "High-power all-fiber-based narrow-linewidth single-mode fiber laser pulses in the C-band and frequency conversion to THz generation," *IEEE J. Quantum Electron.*, vol. 15, no. 2, pp. 377–384, 2009.
[28] G. Yahav *et al.*, "Classification of fluorescent anisotropy decay based on the distance approach in the frequency domain," *Opt. Express*, vol. 30, no. 4, pp. 6176–6192, 2022.
[29] D. Tucker, "Circuits with time-varying parameters (modulators, frequency-changers and parametric amplifiers)," *Radio Electron. Eng.*, vol. 25, no. 3, pp. 263–271, 1963.
[30] N. C. Sagias and G. K. Karagiannidis, "Gaussian class multivariate Weibull distributions: Theory and applications in fading channels," *IEEE Trans. Inf. Theory*, vol. 51, no. 10, pp. 3608–3619, 2005.
[31] K. A. Charles and N. Matthew, *Fundamentals of electric circuits*. McGraw-hill Education, 2017.
[32] R. Simard and P. L'Ecuyer, "Computing the two-sided Kolmogorov-Smirnov distribution," *J. Stat. Softw.*, vol. 39, pp. 1–18, 2011.
[33] A. Taimori *et al.*, "A proper transform for satisfying Benford's law and its application to double JPEG image forensics," in *ISSPIT*. IEEE, 2012, pp. 000 240–000 244.
[34] L. Ljung, "System identification toolbox- Reference," *MATLAB 2022b*.
[35] C. Tofallis, "A better measure of relative prediction accuracy for model selection and model estimation," *J. Oper. Res. Soc.*, vol. 66, pp. 1352–1362, 2015.
[36] G. L. Bretthorst, "An introduction to model selection using probability theory as logic," in *Maximum entropy and Bayesian methods*. Springer, 1996, pp. 1–42.
[37] A. R. Akram *et al.*, "In situ identification of Gram-negative bacteria in human lungs using a topical fluorescent peptide targeting lipid A," *Sci. Transl. Med.*, vol. 10, no. 464, p. eaal0033, 2018.
[38] B. Mills *et al.*, "Molecular detection of gram-positive bacteria in the human lung through an optical fiber–based endoscope," *Eur. J. Nucl. Med. Mol. Imaging*, vol. 48, no. 3, pp. 800–807, 2021.